arXiv:1004.2896v2 [astro-ph.HE] 19 Aug 2011

Gravitational Wave Signatures of Magnetohydrodynamically-Driven Core-Collapse Supernova Explosions

Tomoya Takiwaki[1] and Kei Kotake[1,2]

[1] *Center for Computational Astrophysics, National Astronomical Observatory of Japan, 2-21-1, Osawa, Mitaka, Tokyo, 181-8588, Japan*

[2] *Division of Theoretical Astronomy, National Astronomical Observatory of Japan, 2-21-1, Osawa, Mitaka, Tokyo, 181-8588, Japan*

`takiwaki.tomoya@nao.ac.jp,kkotake@th.nao.ac.jp`

ABSTRACT

By performing a series of two-dimensional, special relativistic magnetohydrodynamic (MHD) simulations, we study signatures of gravitational waves (GWs) in the magnetohydrodynamically-driven core-collapse supernovae. In order to extract the gravitational waveforms, we present a stress formula including contributions both from magnetic fields and special relativistic corrections.

By changing the precollapse magnetic fields and initial angular momentum distributions parametrically, we compute twelve models. As for the microphysics, a realistic equation of state is employed and the neutrino cooling is taken into account via a multiflavor neutrino leakage scheme. With these computations, we find that the total GW amplitudes show a monotonic increase after bounce for models with a strong precollapse magnetic field (10^{12}G) also with a rapid rotation imposed. We show that this trend stems both from the kinetic contribution of MHD outflows with large radial velocities and also from the magnetic contribution dominated by the toroidal magnetic fields that predominantly trigger MHD explosions. For models with weaker initial magnetic fields, the total GW amplitudes after bounce stay almost zero, because the contribution from the magnetic fields cancels with the one from the hydrodynamic counterpart. These features can be clearly understood with a careful analysis on the explosion dynamics. We point out that the GW signals with the increasing trend, possibly visible to the next-generation detectors for a Galactic supernova, would be associated with MHD explosions with the explosion energies exceeding 10^{51} erg.

Subject headings: supernovae: collapse — gravitational waves — neutrinos — hydrodynamics

1. Introduction

Successful detection of neutrinos from SN1987A paved the way for *Neutrino Astronomy* (Hirata et al. 1987; Bionta et al. 1987), alternative to conventional astronomy by electromagnetic waves. Core-collapse supernovae are now expected to be opening yet another astronomy, *Gravitational-Wave Astronomy*. Currently long-baseline laser interferometers LIGO (Abbott et al. 2005), VIRGO[1], GEO600[2], TAMA300 (Ando & the TAMA Collaboration 2005), and AIGO[3] with their international network of the observatories, are beginning to take data at sensitivities where astrophysical events are predicted (see, e.g., Hough et al. (2005) for a recent review). For these detectors, core-collapse supernovae have been proposed as one of the most plausible sources of gravitational waves (GWs) (see, e.g., Kotake et al. (2006); Ott (2009) for recent reviews).

Although the explosion mechanism of core-collapse supernovae has not been completely clarified yet, current multi-dimensional simulations based on refined numerical models show several promising scenarios. Among the candidates is the neutrino heating mechanism aided by convection and standing accretion shock instability (SASI) (e.g., Marek & Janka (2009); Bruenn et al. (2010); Scheck et al. (2004, 2008); Suwa et al. (2009)), the acoustic mechanism (Burrows et al. 2006, 2007b), and the magnetohydrodynamic (MHD) mechanism (e.g., Ardeljan et al. (2000); Kotake et al. (2004a, 2005); Obergaulinger et al. (2006b); Burrows et al. (2007a); Takiwaki et al. (2009) and references therein). For the former two to be the case, the explosion geometry is expected to be unipolar and bipolar, and for the MHD mechanism to be bipolar.

Since the GW signatures imprint a live information of the asphericity at the moment of explosion, they are expected to provide us an important hint to solve the supernova mechanism. So far, most of the theoretical predictions of GWs have focused on the bounce signals in the context of rotational core-collapse (e.g., Mönchmeyer et al. (1991); Zwerger & Mueller (1997); Kotake et al. (2003b); Shibata & Sekiguchi (2004); Ott et al. (2004, 2007a,b); Dimmelmeier et al. (2002a, 2007, 2008); Scheidegger et al. (2008)). For the bounce signals having a strong and characteristic signature, the iron core must rotate enough rapidly. The waveforms are categorized into the following three types, namely types I, II, and III. Type II and III waveforms are shown less likely to appear than type I, because a combination of general relativity (GR) and electron capture near core bounce suppresses multiple bounce in the type II waveforms

---

[1] http://www.ego-gw.it/

[2] http://geo600.aei.mpg.de/

[3] http://www.gravity.uwa.edu.au/

(Dimmelmeier et al. 2007; Ott et al. 2007a,b). In general, a realistic nuclear equation of state (EOS) is stiff enough to forbid the type III waveforms. After bounce, asymmetries due to convection (Burrows & Hayes 1996; Müler & Janka 1997; Fryer 2004; Müller et al. 2004), SASI (Marek et al. 2009; Kotake et al. 2007, 2009b,a; Murphy et al. 2009), and g-mode oscillations of protoneutron stars (Ott et al. 2006), are expected to account for sizable GW signals.

In general, detection of these GW signals in the postbounce phase (except for the g-mode oscillation) is far more difficult than the bounce signals, because they do not possess a clear signature like bounce signals, but change stochastically with time as a result of chaotically growing convection as well as SASI in the non-linear hydrodynamics (Kotake et al. (2009b, 2011); Marek et al. (2009); Murphy et al. (2009)).

Rapid rotation, necessary for the strong bounce signals, is likely to obtain $\sim 1\%$ of massive star population (e.g., Woosley & Bloom (2006)). However this can be really the case for progenitors of rapidly rotating metal-poor stars, which experience the so-called chemically homogeneous evolution (Woosley & Heger 2006; Yoon & Langer 2005). The high angular momentum of the core as well as a strong precollapse magnetic field is preconditioned for the MHD mechanism, because the MHD mechanism relies on the extraction of rotational free energy of the collapsing core via magnetic fields. The energetic MHD explosions are receiving great attention recently as a possible relevance to magnetars and collapsars (e.g., Harikae et al. (2009, 2010) for collective references), which are presumably linked to the formation of long-duration gamma-ray bursts (GRBs) (e.g., Meszaros (2006)).

Among the previous studies mentioned above, only a small portion of papers has been spent on determining the GW signals in the MHD mechanism (Yamada & Sawai 2004; Kotake et al. 2004b; Obergaulinger et al. 2006b; Cerdá-Durán et al. 2007; Shibata et al. 2006; Scheidegger et al. 2010). This may be because the MHD effects on the dynamics as well as their influence over the GW signals can be visible only for cores with precollapse magnetic fields over $B_0 \gtrsim 10^{12}$ G (Obergaulinger et al. 2006b; Kotake et al. 2004b). Considering that the typical magnetic-field strength of GRB progenitors is at most $\sim 10^{11-12}$ G (Woosley & Heger 2006), this is already an extreme situation. Interestingly in a more extremely case of $B_0 \sim 10^{13}$ G, a secularly growing feature in the waveforms was observed (Obergaulinger et al. 2006a; Shibata et al. 2006; Scheidegger et al. 2010). Moreover Obergaulinger et al. (2006a) called a waveform as type IV in which quasi-periodic large-scale oscillations of GWs near bounce are replaced by higher frequency irregular oscillations. Some of these MHD simulations follow adiabatic core-collapse, in which a polytropic EOS is employed to mimic supernova microphysics. At this level of approximation, the bounce shock generally does not stall and a prompt explosion occurs within a few ten milliseconds after bounce. Therefore a main focus in these previous studies has been rather limited to the early postbounce phase ($\lesssim$ several 10 ms). However, for models with weaker precollapse magnetic fields akin to the current GRB progenitors, the prompt shocks stall firstly in the core like a conventional supernova model with more sophisticated neutrino treatment (e.g., Burrows et al. (2007a)). In such a case, the onset of MHD explosions, depending on the initial rotation rates, can be delayed till $\sim$ 100 ms after bounce (Burrows et al. 2007a; Takiwaki et al. 2009). There remains a room to study GW signatures in such a case, which we hope to study in this work.

In this study, we choose to take precollapse magnetic fields less than 10^{12} G based on a recent GRB-oriented progenitor models. By this choice, it generally takes much longer time after bounce than the adiabatic MHD models to amplify magnetic fields enough strong to overwhelm the ram pressure of the accreting matter, leading to the magnetohydrodynamically-driven (MHD, in short) explosions. Even if the speed of jets in MHD explosions is only mildly relativistic, Newtonian simulations are not numerically stable because the Alfvén velocity ($\propto B/\sqrt{\rho}$) could exceed the speed of light unphysically especially when the strongly magnetized jets (i.e., large B) propagate to a stellar envelope with decreasing density (ρ). To follow a long-term postbounce evolution numerically stably, we perform special relativistic MHD (SRMHD) simulations (Takiwaki et al. 2009), in which a realistic EOS is employed and the neutrino cooling is taken into account via a multiflavor neutrino leakage scheme. Note in our previous study of GWs in magneto-rotational core-collapse (Kotake et al. 2004b) that we were unable to study properties of the GWs long in the postbounce phase because the employed Newtonian simulations quite often crashed especially in the case of strong MHD explosions. To include GR effects in this study, we follow a prescription in Obergaulinger et al. (2006a) which is reported to capture basic features of full GR simulations quite well. By changing precollapse magnetic fields as well as initial angular momentum distributions parametrically, we compute twelve models. By doing so, we hope to study the properties of GWs in MHD explosions systematically and also address their detectability.

The paper opens up with descriptions of the initial models and numerical methods employed in this work (section 2). Formalism for calculating the gravitational waveforms in SRMHD is summarized in section 3. The main results are given in Section 4. We summarize our results and discuss their implications in Section 5.

2. Models and Numerical Methods

2.1. Initial Models

We make precollapse models by taking the profiles of density, internal energy, and electron fraction distribution from a rotating presupernova model of E25 in Heger & Langer (2000). This model has mass of $25M_{\odot}$ at the zero-age main sequence, however loses the hydrogen envelope and becomes a Wolf-Rayet (WR) star of 5.45 $M_{\odot}$ before core-collapse. Our computational domain involves the whole iron-core of $1.69M_{\odot}$. Note that this model is suggested as a candidate progenitor of long-duration GRBs because type Ib/c core-collapse supernovae originated from WR stars have a observational association with long-duration GRBs (e.g., Woosley & Bloom (2006)).

Since little is known about the spatial distributions of rotation and magnetic fields in evolved massive stars, we add the following profiles in a parametric manner to the non-rotating core mentioned above. For the rotation profile, we assume a cylindrical rotation of

$$\Omega(X,Z) = \Omega_0 \frac{X_0^2}{X^2+X_0^2}\frac{Z_0^4}{Z^4+Z_0^4}, \tag{1}$$

where Ω is angular velocity and X and Z denotes distance from the rotational axis and the equatorial plane, respectively. The parameter X_0 represents the degree of differential rotation, which we choose to change in the following three ways, 100km (strongly differential rotation), 500km, (moderately differential rotation), and 2000km (uniform rotation), respectively. The parameter Z_0 is fixed to 1000km.

Regarding the precollapse magnetic field, we assume that the magnetic field is nearly uniform and parallel to the rotational axis in the core and dipolar outside. This can be modeled by the following effective vector potential,

$$A_r = A_\theta = 0, \tag{2}$$

$$A_\phi = \frac{B_0}{2}\frac{r_0^3}{r^3+r_0^3} r\sin\theta, \tag{3}$$

where $A_{r,\theta,\phi}$ is vector potential in the r, θ, ϕ direction, respectively, r is radius, r_0 is radius of the core, and B_0 is a model constant (see Takiwaki et al. (2004) for detail). In this study, r_0 is set to 2000 km which is approximately the size of the precollapse iron core.

By changing initial angular momentum, degree of differential rotation, and the strength of magnetic fields, we compute twelve models. The model parameters are shown in Table 1.

The models are named after this combination, with the first letters, B12, B11 representing strength of the initial magnetic field, the second letters, $X1, X5, X20$ indicating the degree of differential rotation ($X_0 = 100, 500, 2000$ km, respectively), and the third letter, $\beta = 0.1, 1$ showing the rotation parameter β. Here β represents ratio of the rotational energy to the absolute value of the gravitational energy prior to core-collapse. The original progenitor of model E25 in Heger & Langer (2000) has a uniform rotation profile in the iron core and the initial β parameter is ~ 0.15 %. So the initial angular momentum in our models of B11X20β0.1 and B12X20β0.1 are similar to the original one. In a GRB-oriented progenitor of model 35OB (Woosley & Heger 2006), the precollapse magnetic fields reach to $\sim 10^{11} - 10^{12}$ G and $\beta \sim 0.2\%$, which is not so different from the chosen parameters here. Although little is known about the degree of precollapse differential rotation, an extremely strong one, for example, our model series of X1, should be unrealistic. These models, albeit rather academic, are examined in order to see clearly the effects of differential rotation.

	β(%)					
	0.1%			1%		
	X_0(km)					
	100km	500km	2000km	100km	500km	2000km
B_0 : 10^{11}G	B11X1β0.1	B11X5β0.1	B11X20β0.1	B11X1β1	B11X5β1	B11X20β1
10^{12}G	B12X1β0.1	B12X5β0.1	B12X20β0.1	B12X1β1	B12X5β1	B12X20β1

Table 1: Summary of initial models. Model names are labeled by the precollapse magnetic fields and rotation. β represents ratio of initial rotational energy to the absolute value of the initial gravitational energy. From left to right in the table, Ω_0 in unit of rad/s (equation (1)) is 24, 2.8, 0.95, 76, 8.9, and 3.0, respectively. Note that X_0 and B_0 is defined in equation (1) and (3), respectively.

2.2. Special Relativistic Magnetohydrodynamics

Numerical results in this work are calculated by the SRMHD code developed in Takiwaki et al. (2009). In the following, we first mention the importance of SR and then briefly summarize the numerical schemes.

The Alfvén velocity of MHD jets propagating into the outer layer of the iron core can be estimated as $v_A \sim 10^{10}$cm/s $(B/10^{13}\text{G})(\rho/10^5\text{g/cm}^3)^{-1/2}$, where ρ and B are the typical density and the magnetic field near along the rotational axis. It can be readily inferred that the Alfvén velocity could exceed the speed of light unphysically in Newtonian simulations.

SR corrections are also helpful to capture correctly the dynamics of infalling material in the vicinity of the protoneutron star, because their free-fall velocities and rotational velocities become close to the speed of light. Such conditions are quite ubiquitous in MHD explosions. Even if the propagation speeds of the jets are only mildly relativistic, we have learned that (at least) SR treatments are quite important for keeping the stable numerical calculations in good accuracy over a long-term postbounce evolution (e.g., Harikae et al. (2009)).

The MHD part of our code is based on the formalism of De Villiers et al. (2003). The state of the relativistic fluid element at each point in the space time is described by its density, ρ; specific energy, e; velocity, v^i; and pressure, p. And the magnetic field in the laboratory frame is described by the four-vector $\sqrt{4\pi}b^\mu = {}^*F^{\mu\nu}U_\nu$, where ${}^*F^{\mu\nu}$ is the dual of the electro-magnetic field strength tensor and U_ν is the four-velocity. The basic equations of the SRMHD code are written as,

$$\frac{\partial D}{\partial t} + \frac{1}{\sqrt{\gamma}}\partial_i\sqrt{\gamma}Dv^i = 0 \tag{4}$$

$$\frac{\partial E}{\partial t} + \frac{1}{\sqrt{\gamma}}\partial_i\sqrt{\gamma}Ev^i = -p\frac{\partial W}{\partial t} - \frac{p}{\sqrt{\gamma}}\partial_i\sqrt{\gamma}Wv^i - \mathcal{L}_\nu \tag{5}$$

$$\begin{aligned}\frac{\partial(S_i - b^t b_i)}{\partial t} + \frac{1}{\sqrt{\gamma}}\partial_j\sqrt{\gamma}\left(S_i v^j - b_i b^j\right) = & -\frac{1}{2}\left(\rho h\left(Wv_k\right)^2 - (b_k)^2\right)\partial_i\gamma^{kk} \\ & - \left(\rho h W^2 - {b^t}^2\right)\partial_i\Phi_{\rm tot} \\ & -\partial_i\left(p + \frac{|b|^2}{2}\right)\end{aligned} \tag{6}$$

$$\frac{\partial(Wb^i - Wb^t v^i)}{\partial t} + \partial_j\left(Wv^j b^i - Wv^i b^j\right) = 0 \tag{7}$$

$$\begin{aligned}\partial^k\partial_k\Phi = & \, 4\pi\Big[\rho h(W^2 + (v_k)^2) + 2\left(p + \frac{|b|^2}{2}\right) \\ & - \left((b^0)^2 + (b_k)^2\right)\Big]\end{aligned} \tag{8}$$

where $W = \frac{1}{\sqrt{1 - v^k v_k}}$, $D = \rho W$, $E = eW$ and $S_i = \rho h W^2 v_i$ are the Lorentz boost factor, auxiliary variables correspond to density, energy, and momentum, respectively. All of them are defined in the laboratory frame. Equations (4,5,6) represents the mass, energy, and momentum conservation, respectively. In equation (6), note that the relativistic enthalpy, $h = (1 + e/\rho + p/\rho + |b|^2/\rho)$ includes the magnetic energy. Equation (7) is induction equation in SR. In solving the equation, the method of characteristics is implemented to propagate accurately all modes of MHD waves (see Takiwaki et al. (2009) for more detail). Equation

(8) is Poisson equation for the gravitational potential of Φ, which is solved by the modified incomplete Cholesky conjugate gradient method. For an approximate treatment of general relativistic (GR) gravity, $\Phi_{\rm tot}$ in equation (6) includes a GR correction to Φ as in Buras et al. (2006). We employ a realistic equation of state based on the relativistic mean field theory (Shen et al. 1998).

We approximate the neutrino cooling by a neutrino multiflavor leakage scheme (Epstein & Pethick 1981; Rosswog & Liebendörfer 2003), in which three neutrino flavors: electron neutrino(ν_e), electron antineutrino($\bar{\nu}_e$), and heavy-lepton neutrinos(ν_μ, $\bar{\nu}_\mu$, ν_τ, $\bar{\nu}_\tau$, collectively referred to as ν_X), are taken into account. The implemented neutrino reactions are electron capture on proton and free nuclei; positron capture on neutron; photo-, pair, plasma processes (Fuller et al. 1985; Takahashi et al. 1978; Itoh et al. 1989, 1990). A transport equation for the lepton fractions (namely $Y_e - Y_{e^+}, Y_{\nu_e}, Y_{\bar{\nu}_e}$ and Y_{ν_X}, are solved in an operator-splitting manner (see equation (7) in Takiwaki et al. (2009) for more detail). $\mathcal{L}_\nu$ in equation (5) represents the neutrino cooling rate summed over all the reactions, which can be also estimated by the leakage scheme (see Epstein & Pethick (1981); Rosswog & Liebendörfer (2003); Kotake et al. (2003a) for more detail).

In our two dimensional simulations, the spherical coordinates are employed with $300(r) \times 60(\theta)$ grid points to cover the computational domain assuming axial and equatorial symmetry. The radial grid is nonuniform, extending from 0 to 4000km with finer grid near the center. The finest grid for the radial direction is set to 1km. The polar grid uniformly covers from $\theta = 0$ to $\pi/2$. The finest grid for the polar direction is 25 m. The numerical tests and convergence with this choice of the numerical grid points are given in section 5 of Takiwaki et al. (2009).

To measure the strength of explosion, we define the explosion energy as follows,

$$E_{\rm exp} = \int_{\rm D} dV\ e_{\rm local} = \int_{\rm D} dV \left(e_{\rm kin} + e_{\rm int} + e_{\rm mag} + e_{\rm grav}\right), \tag{9}$$

here $e_{\rm local}$ is the sum of $e_{\rm kin}$, $e_{\rm int}$, $e_{\rm mag}$ and $e_{\rm grav}$ with being kinetic, internal, magnetic, and gravitational energy, respectively defined as

$$\begin{aligned} e_{\rm kin} &= \rho W\left(W-1\right), & (10)\\ e_{\rm int} &= eW^2 + p\left(W^2-1\right), & (11)\\ e_{\rm mag} &= |b|^2\left(1-\frac{1}{2W^2}\right) - \frac{b^{0^2}}{2W^2}, & (12)\\ e_{\rm grav} &= -\rho h W^2 \Phi, & (13)\end{aligned}$$

and D in equation (9) represents the domain where the local energy ($e_{\rm local}$) is positive, indicating that the matter is gravitationally unbound. The explosion energy is evaluated when the MHD jets pass through 1000 km along the polar direction.

3. Formulae for Gravitational Waves in SRMHD

To extract the gravitational waveforms in MHD explosions, we present the stress formula in SRMHD for later convenience. As shown below, this can be done straightforwardly by extending the Newtonian MHD formulation presented in Kotake et al. (2004b).

From the Einstein equation, one obtains the following formula as a primary expression for the leading part of the gravitational quadrupole field emitted by the motion of a fluid in the post-Newtonian approximation (e.g., Mönchmeyer et al. (1991); Finn & Evans (1990); Blanchet et al. (1990)),

$$h^{TT}_{ij}(\boldsymbol{X},t) = \frac{4G}{c^4 R} P_{ijkl}(\boldsymbol{N}) \int d^3x \; T_{kl}, \tag{14}$$

where G and c are the gravitational constant and the velocity of light, respectively, T_{kl} is the energy momentum tensor of the source, $R \equiv (\delta_{ij} X^i X^j)^{1/2} = |\boldsymbol{X}|$ is the distance between the observer and the source. P_{ijkl}, with $\boldsymbol{N} = \boldsymbol{X}/R$ denotes the transverse-traceless (TT) projection operator onto the plane orthogonal to the outgoing wave direction $\boldsymbol{N}$ (e.g., Mönchmeyer et al. (1991)) .

T_{ij} consists of the three parts, namely of perfect fluid, electromagnetic field, and gravitational potential as follows,

$$T_{ij} = T_{ij\,(\mathrm{hyd})} + T_{ij\,(\mathrm{mag})} + T_{ij\,(\mathrm{grav})}. \tag{15}$$

The first term which we refer as the hydrodynamic part is explicitly written as,

$$T_{ij\,(\mathrm{hyd})} = \rho_* W^2 v_i v_j + p\delta_{ij}, \tag{16}$$

where ρ_* is effective density defined as,

$$\rho_* = \rho + \frac{e + p + |b|^2}{c^2}. \tag{17}$$

The second term in equation (15) represents the contribution from magnetic fields as,

$$T_{ij\,(\mathrm{mag})} = -b_i b_j. \tag{18}$$

And the last term in equation (15) is the contribution from the gravitational potential,

$$T_{ij\,(\mathrm{grav})} = \frac{1}{4\pi G}\left(\Phi_{,i}\Phi_{,j} - \frac{1}{2}\delta_{ij}\Phi_{,m}\Phi^{,m}\right) \tag{19}$$

where Φ corresponds to the self-gravity in equation (8).

In our axisymmetric case, there remains only one non-vanishing quadrupole term in the metric perturbation, namely $\ell = 2, m = 0$ in terms of the pure-spin tensor harmonics, as

$$h_{ij}^{TT}(\boldsymbol{X}, t) \overset{\ell=2,m=0}{=} \frac{1}{R} A_{20}^{E2}\left(t - \frac{R}{c}\right) T_{ij}^{E2,20}(\theta, \phi), \tag{20}$$

where $T_{ij}^{E2,20}(\theta, \phi)$ is

$$T_{ij}^{E2,20}(\theta, \phi) = \frac{1}{8}\sqrt{\frac{15}{\pi}} \sin^2\theta, \tag{21}$$

(e.g., Thorne (1980)). The projection operator in equation (14) acts on T_{ij} as,

$$P_{ijkl}T^{kl} = 2T^{zz} - T^{xx} - T^{yy}. \tag{22}$$

Transforming equation (14) to the spherical coordinates, and expressing b_i and v_i in terms of unit vectors in the r, θ, ϕ direction, we obtain for A_{20}^{E2} the expression,

$$A_{20}^{\mathrm{E2}} = A_{20\,(\mathrm{hyd})}^{\mathrm{E2}} + A_{20\,(\mathrm{mag})}^{\mathrm{E2}} + A_{20\,(\mathrm{grav})}^{\mathrm{E2}}, \tag{23}$$

where

$$\begin{aligned} A_{20\,(\mathrm{hyd})}^{\mathrm{E2}} &= \frac{G}{c^4}\frac{32\pi^{3/2}}{\sqrt{15}} \int_0^1 d\mu \int_0^\infty r^2\, dr f_{20\,(\mathrm{hyd})}^{\mathrm{E2}}, && (24)\\ f_{20\,(\mathrm{hyd})}^{\mathrm{E2}} &= \rho_* W^2({v_r}^2(3\mu^2-1) + {v_\theta}^2(2-3\mu^2) - {v_\phi}^2 - 6v_r v_\theta\,\mu\sqrt{1-\mu^2}); && (25)\end{aligned}$$

$$\begin{aligned} A_{20\,(\mathrm{grav})}^{\mathrm{E2}} &= \frac{G}{c^4}\frac{32\pi^{3/2}}{\sqrt{15}} \int_0^1 d\mu \int_0^\infty r^2\, dr f_{20\,(\mathrm{grav})}^{\mathrm{E2}}, && (26)\\ f_{20\,(\mathrm{grav})}^{\mathrm{E2}} &= \left[\rho h(W^2 + (v_k/c)^2) + \frac{2}{c^2}\left(p + \frac{|b|^2}{2}\right) - \frac{1}{c^2}\left((b^0)^2 + (b_k)^2\right)\right] \\ &\quad \times\left[-r\partial_r\Phi(3\mu^2-1) + 3\partial_\theta\Phi\,\mu\sqrt{1-\mu^2}\right]; && (27)\end{aligned}$$

and

$$\begin{aligned} A_{20\,(\mathrm{mag})}^{\mathrm{E2}} &= -\frac{G}{c^4}\frac{32\pi^{3/2}}{\sqrt{15}} \int_0^1 d\mu \int_0^\infty r^2\, dr f_{20\,(\mathrm{mag})}^{\mathrm{E2}}, && (28)\\ f_{20\,(\mathrm{mag})}^{\mathrm{E2}} &= [{b_r}^2(3\mu^2-1) + {b_\theta}^2(2-3\mu^2) - {b_\phi}^2 - 6b_r b_\theta\mu\sqrt{1-\mu^2}]; && (29)\end{aligned}$$

where $\mu = \cos\theta$. For later convenience, we write the total GW amplitude as,

$$h^{\mathrm{TT}} = h_{(\mathrm{hyd})}^{\mathrm{TT}} + h_{(\mathrm{mag})}^{\mathrm{TT}} + h_{(\mathrm{grav})}^{TT}, \tag{30}$$

where the quantities of the right hand are defined by combining equations (20) and (23) with equations (25), (27), and (29). By dropping $O(v/c)$ terms, the above formulae reduce to the conventional Newtonian stress formula (e.g., Mönchmeyer et al. (1991)). In the following computations, the observer is assumed to be located in the equatorial plane ($\theta = \pi/2$ in equation (21)), and that the source is located near at our galactic center ($R = 10$ kpc).

4. Results

The gravitational waveforms obtained in this work can be categorized into two, which we call increasing type or cancellation type just for convenience. Note that the latter type does not mean a new waveform as will be explained later in this section. Regarding the former one, such a waveform was presented in previous literature (Obergaulinger et al. 2006a; Shibata et al. 2006; Scheidegger et al. 2010), however their properties have not been clearly understood yet. In section 4.1, we first overview their characters, which are peculiar in the case of MHD explosions. In section 4.2, we move on to analyze their properties by carefully comparing each contribution in equation (30) to the total GW amplitudes. Then in section 4.3, we perform the spectra analysis and discuss their detectability.

4.1. Properties of Waveforms in the MHD Exploding Models

Figure 1 shows examples of the two categories, which we call as the increasing (left panels) or cancellation type (right panels), respectively. In the increasing type, the total wave amplitudes (red line) have a monotonically increase trend after bounce ($t - t_b = 0$ in the figures). While in the cancellation type (right panels), the total amplitudes after bounce stay almost zero. This is because the contribution from the magnetic fields (blue line, equation (29)) cancels with the one from the sum of the hydrodynamic and gravitational parts (green line, equations (25,27)). Regardless of the difference in the two types, it is common that the magnetic contribution (blue line) increases almost monotonically with time. Not surprisingly, the bounce GW signals (($t - t_b \lesssim 20$ ms) are categorized into the so-called type I or II waveforms. Note here that the MHD simulations are terminated at around 100 ms after bounce for all the computed models. This is simply because the GW amplitudes in a more later phase decrease because the MHD shock comes out of the computational domain and the enclosed mass in the domain becomes smaller.

Table 2 depicts a classification of the computed models, in which "C" and "I" indicates the cancellation and increasing type, respectively. I* in the table indicates the mixture of the two types, which we call as intermediate type. The table shows that the bifurcation of the two types is predominantly determined by the precollapse magnetic fields, so that the models with stronger magnetic fields (B_0 10^{12} G) are basically classified to the increasing type. For models colored by orange, which are slow rotator with uniform rotation in our models, the field amplification works less efficiently than for models with stronger differential rotation (such as $X_0 = 100, 500$ km) (see also Cerdá-Durán et al. (2008)). This suppresses the increase in the wave amplitudes due to magnetic fields, which gives rise to the intermediate state between the two types.

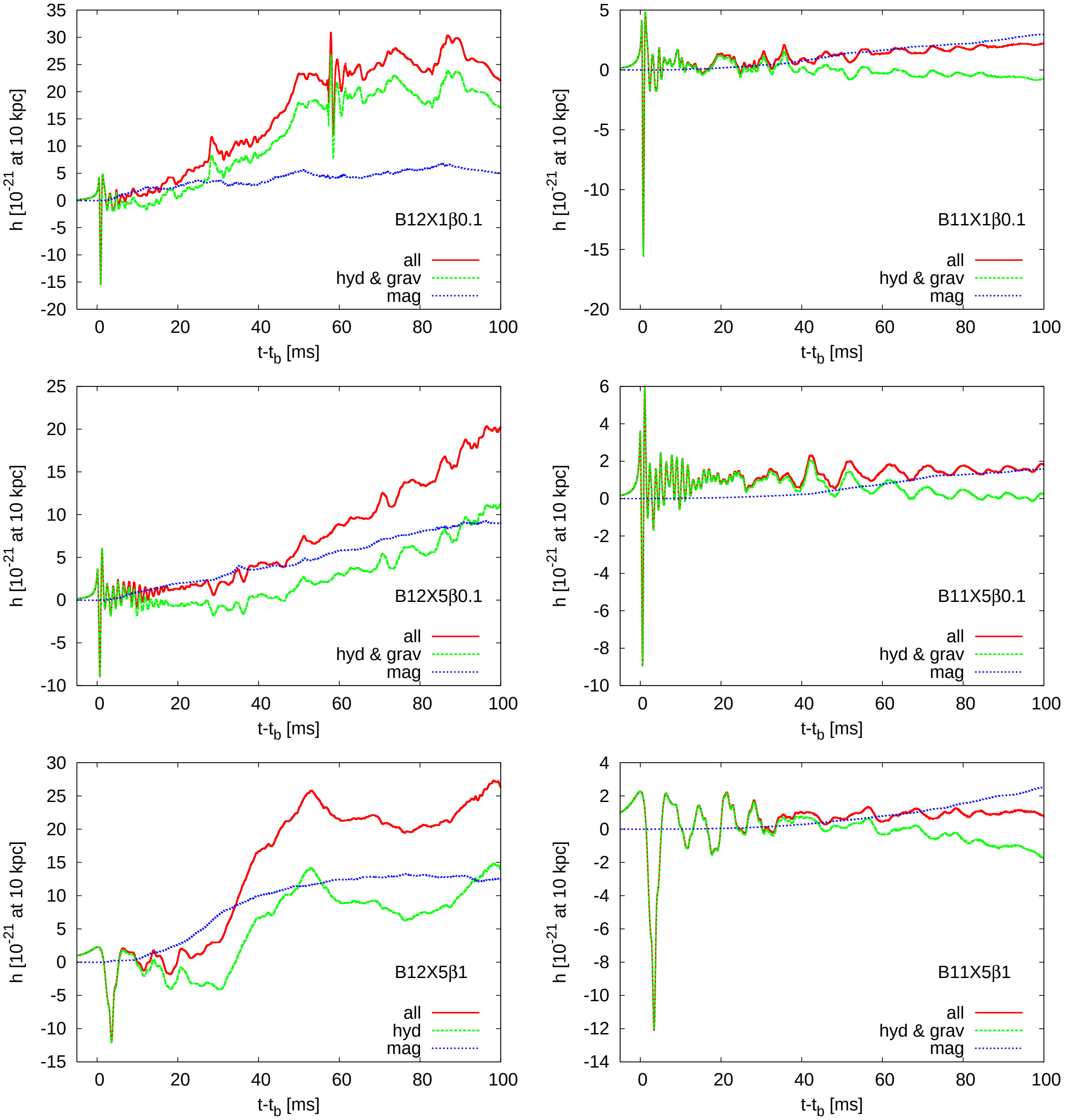

Fig. 1.— Gravitational waveforms with the increasing (left) or the cancellation trend (right) (see text for more detail). At the right bottom in each panel, the model names are given such as B12X1β0.1 (top left, for example). The total wave amplitudes are shown by the red line, while the contribution from the magnetic fields and from the sum of the hydrodynamic and gravitational parts are shown by blue and green lines, respectively (e.g., equation (29) and equations (25,27)).

Table 3 is a summary showing intervals measured from the stall of the bounce shock (top) and from core bounce (bottom) till the MHD-driven revival of the stalled bounce shock. As already mentioned in Takiwaki et al. (2009), generation of the postbounce MHD jets proceeds in the following two ways. One is launched relatively promptly after the stall of the bounce shock, typically earlier than ~ 30 ms (see models colored by red in Table 3) and another is launched rather later after bounce ($\gtrsim 30$ ms) (models colored by green in Table 3). In this sense, our computed models could be roughly categorized into two, namely promptly MHD explosion (colored by red in Table 3) or delayed MHD explosion (colored by green in Table 3), respectively. This simply reflects that it takes longer time for the weakly magnetized models to amplify the magnetic pressure behind the stalled shock enough strong to overwhelm the ram pressure of accreting matter. By comparing Table 2 to 3, the two characters in the waveforms have a rough correlation with the difference of the explosion dynamics.

Table 4 shows a summary regarding the explosion energy (e.g., equation (9)). Comparing Table 2 to 4, the explosion energy for the increasing type (models colored by yellow in Table 2 and 4) is higher compared to the cancellation type (models colored by light blue). Given the rotation rate of $\beta = 0.1\%$, the explosion energy is smallest for the intermediate type (models colored by orange) due to the insufficient field amplification as mentioned above. It can be also shown that the explosion energies for the models with the increasing trend generally exceed 10^{51} erg (models colored by yellow).

Having summarized the waveform classification together with the explosion dynamics, we move on to look more in detail what makes the difference between the two types in the next section.

		$\beta_{\rm rot}$(%)					
		0.1%			1%		
		X_0(km)					
		100km	500km	2000km	100km	500km	2000km
B_0(Gauss)	10^{11}G	C	C	I*	C	C	C
	10^{12}G	I	I	I*	I	I	I

Table 2: Same as Table 1 but for the classification of the computed models. "C" and "I" indicates the cancellation and increasing type, respectively, while I* indicates the mixture of the two types, which we refer to as intermediate type.

		$\beta_{\rm rot}(\%)$					
		0.1%			1%		
		X_0(km)					
		100km	500km	2000km	100km	500km	2000km
B_0(Gauss)	10^{11}G	🟩 38ms	🟩 57ms	🟩 91ms	🟥 18ms	🟩 87ms	🟩 75ms
	10^{12}G	🟥 7ms	🟥 18ms	🟥 28ms	🟥 3ms	🟥 17ms	🟥 19ms

		$\beta_{\rm rot}(\%)$					
		0.1%			1%		
		X_0(km)					
		100km	500km	2000km	100km	500km	2000km
B_0(Gauss)	10^{11}G	🟩 40ms	🟩 58ms	🟩 92ms	🟥 25ms	🟩 95ms	🟩 81ms
	10^{12}G	🟥 10ms	🟥 20ms	🟥 30ms	🟥 8ms	🟥 20ms	🟥 22ms

Table 3: Same as Table 1 but for the interval measured from the stall of the bounce shock to the MHD-driven revival of the stalled shock (top panel) and the one measured from core bounce (bottom panel). The computed models are classified whether the launch of the MHD jets occurs relatively promptly after bounce (models colored by red, with the intervals being shorter than ~ 30 ms typically) or rather later (models colored by green), which we refer to as promptly or delayed MHD explosion for convenience in this work (see text for more detail). Note that these timescales are estimated just by looking at the velocity evolutions along the polar axis.

		$\beta_{\rm rot}(\%)$					
		0.1%			1%		
		X_0(km)					
		100km	500km	2000km	100km	500km	2000km
B_0(Gauss)	10^{11}G	🟦 8×10^{49}	🟦 5×10^{48}	🟧 2×10^{48}	🟦 3×10^{50}	🟦 2×10^{47}	🟦 2×10^{48}
	10^{12}G	🟨 2.5×10^{51}	🟨 2×10^{51}	🟧 4×10^{50}	🟨 4×10^{51}	🟨 3×10^{51}	🟨 1.5×10^{51}

Table 4: Same as Table 1 but for the explosion energy (defined in equation (9)). Comparing with Table 2 to 4, the explosion energies for the models with the increasing trend generally exceed 10^{51} erg (models colored by yellow). [1]

4.2. Analysis of Waveforms

4.2.1. Increasing type

By taking model B12X1β0.1 as a reference, we first focus on the increase-type waveform. The left panel of Figure 2 depicts distributions of entropy (left-half) and plasma β (right-half, the ratio of matter to magnetic pressure) at 100 ms after bounce. It can be seen that the outgoing jets indicated by the velocity fields (arrows in the left-half) are driven by the magnetic pressure behind the shock (see bluish region (i.e., low plasma β) in the right-half panel).

The right panel of Figure 2 shows contributions to the total GW amplitudes (equation (27)), in which the left-hand-side panels are for the sum of the hydrodynamic and gravitational part, namely $\log\left(\pm\left[f^{\rm E2}_{20\,({\rm hyd})}+f^{\rm E2}_{20\,({\rm grav})}\right]\right)$ (left top(+)/bottom(−)(equations (25,27)), and the right-hand-side panels are for the magnetic part, namely $\log\left(\pm f^{\rm E2}_{20\,({\rm mag})}\right)$ (right top(+)/bottom(−)) (e.g., equation (29)). By comparing the top two panels in Figure 2, it can be seen that the positive contribution is overlapped with the regions where the MHD outflows exist. The major positive contribution is from the kinetic term of the MHD outflows with large radial velocities (e.g., $+\rho_* W^2 {v_r}^2$ in equation (25)). The magnetic part also contributes to the positive trend (see top right-half in the right panel (labeled by mag(+))). This comes from the toroidal magnetic fields (e.g., $+{b_\phi}^2$ in equation (29)), which dominantly contribute to drive MHD explosions. The magnetic contribution was already mentioned in Kotake et al. (2004b). This study furthermore adds that the kinetic energy of MHD outflows more importantly contributes to the positive trend.

Figure 3 shows a normalized cumulative contribution of each term in $A^{\rm E2}_{20}$, which is estimated by the volume integral of $A^{\rm E2}_{20}$ within a given sphere enclosed by certain radius. It can be seen that the contribution of the hydrodynamic and gravity parts (indicated by "hyd & grav") is prominent for radius outside $\sim$ 1000 km, which stems from exploding regions with large kinetic energy as mentioned above. Note that the secular drift observed in the increase-type waveform may come from ambiguities in estimating the gravitational potential in the stress formula as pointed out by Dimmelmeier et al. (2002b). To exclude such potential issues, we plot the waveform calculated by the first-moment of momentum-density formalism (e.g., Finn & Evans (1990)). As is shown in Figure 4, the increasing trend is also seen in the waveform estimated by the first-moment formalism (green line). As a side-remark, a more smoother curve is obtained for the stress formula (red line), about which Mönchmeyer et al. (1991) pioneeringly mentioned that the numerical evaluation of the time-derivative sometimes makes the waveform noisy.[1]

4.2.2. Cancellation type

Now we proceed to focus on the cancellation-type waveform by taking model B11X1β1 as an example. Top panel in Figure 5 shows density distributions (left-half) with the plasma β (right-half). Note that the jet head of MHD outflows is located at ~ 400 km along the pole which sticks out of the plots in Figure 5 (compare the difference in scales of Figure 2). In fact, the bluish regions (low β) around the pole have a lower density because material there has been already blown up due to the passage of MHD-driven shocks. The middle panel of Figure 5 shows the term-by-term contribution to A_{20}^{E2} as in the right panel of Figure 2. From the right-half panel, it is shown that the magnetic contribution dominantly makes a positive contribution (labeled by mag(+)), which is also the case of the increasing type as mentioned in the previous section. Note that the negative contribution from magnetic fields (bluish region in the bottom-right-half of the middle panel) comes from the regions, where are off-axis from the propagation of the MHD jets. In these regions, the poloidal components of magnetic fields are stronger than the toroidal ones, which makes the negative contribution mainly through $-[{b_r}^2(3\mu^2-1)+{b_\theta}^2(2-3\mu^2)]$ in equation (29).

Looking at the sum of the hydrodynamic and gravitational part (left-half in the middle panel), a large negative contribution comes from regions near in the rotational axis (colored by red, bottom-left-half). The bottom panel of Figure 5 further shows a contribution from the hydrodynamic (left-half) and gravitational part (right-half), separately. Regarding the hydrodynamic part, the negative contribution is highest in the vicinity of the equatorial plane which closely coincides with the oblately deformed protoneutron star (colored by red, the bottom-left-half in the bottom panel). This is because the negative contribution comes from the centrifugal forces (e.g., the term related to the rotational energy, $-\rho {v_\phi}^2$ in equation (25)). For the gravity part (right-half in the bottom panel), a big negative contribution comes from regions in the vicinity of the rotational axis (bottom-right-half). This comes from the term of $-r\partial_r\Phi(3\mu^2-1)$ in equation (25), which is the radial gradient of the gravitational potential. Remembering that $\partial_r\Phi > 0$ is generally satisfied in self-gravitating objects, the sign of this term is determined by $\mu = \cos\theta$ which is a directional cosine measured from the rotational axis. As a result, the gravity part makes a negatively contribution in the vicinity of the rotational axis ($\mu \sim 1$). These two factors coming both from the hydrodynamic and gravity part make the negative contribution to the GW amplitudes. In fact, the negative

---

[1] This may be the reason why the stress formula has been often employed in supernova researches so far.

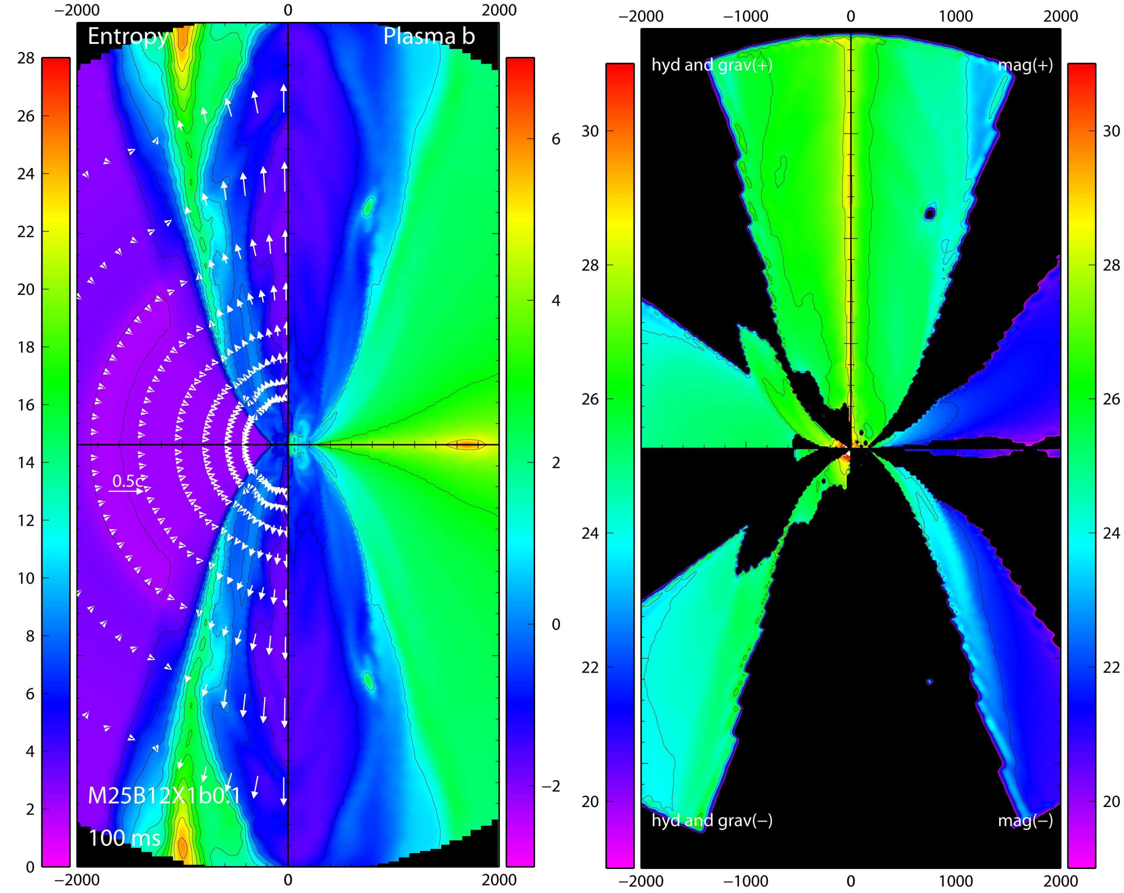

Fig. 2.— Left panel shows distributions of entropy [k_B/baryon] (left) and logarithm of plasma β (right) for model B12X1β0.1 at 100ms after bounce. The white arrows in the left-hand side show the velocity fields, which are normalized by the scale in the middle left edge (0.5c). Right panel shows the sum of the hydrodynamic and gravitational parts (indicated by "hyd and grav" in the left-hand side) and the magnetic part (indicated by "mag" in the right-hand side), respectively. The top and bottom panels represent the positive and negative contribution (indicated by (+) or (-)) to A_{20}^{E2}, respectively (see text for more detail). The side length of each plot is 4000(km)x8000(km).

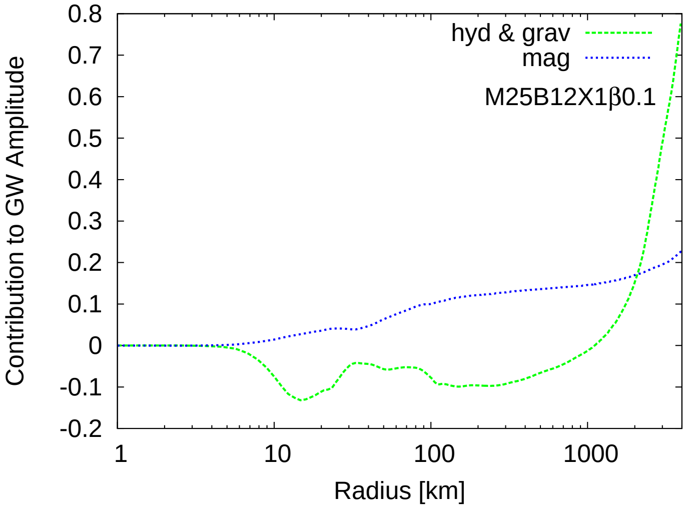

Fig. 3.— Normalized cumulative contribution of each term in $A_{20}^{\rm E2}$ as a function of radius for model B12X1β0.1. This is estimated by the volume integral of $A_{20}^{\rm E2}$ within sphere of a given radius.

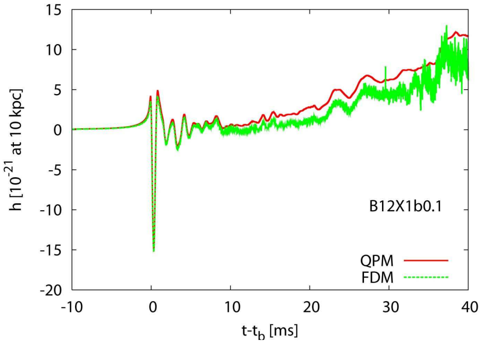

Fig. 4.— Gravitational waveform extracted either by the stress formula (indicated by QPM, red line) or by the first-moment of momentum-density formalism (FDM, green line) for model B12X1β0.1), respectively.

contribution is highest near at the surface of the protoneutron star ($\sim$ 10 km in Figure 6). Outside it, the magnetic part becomes almost comparable to the sum of the hydrodynamic and gravity part, which makes the cancellation type shown in the right panels of Figure 1.

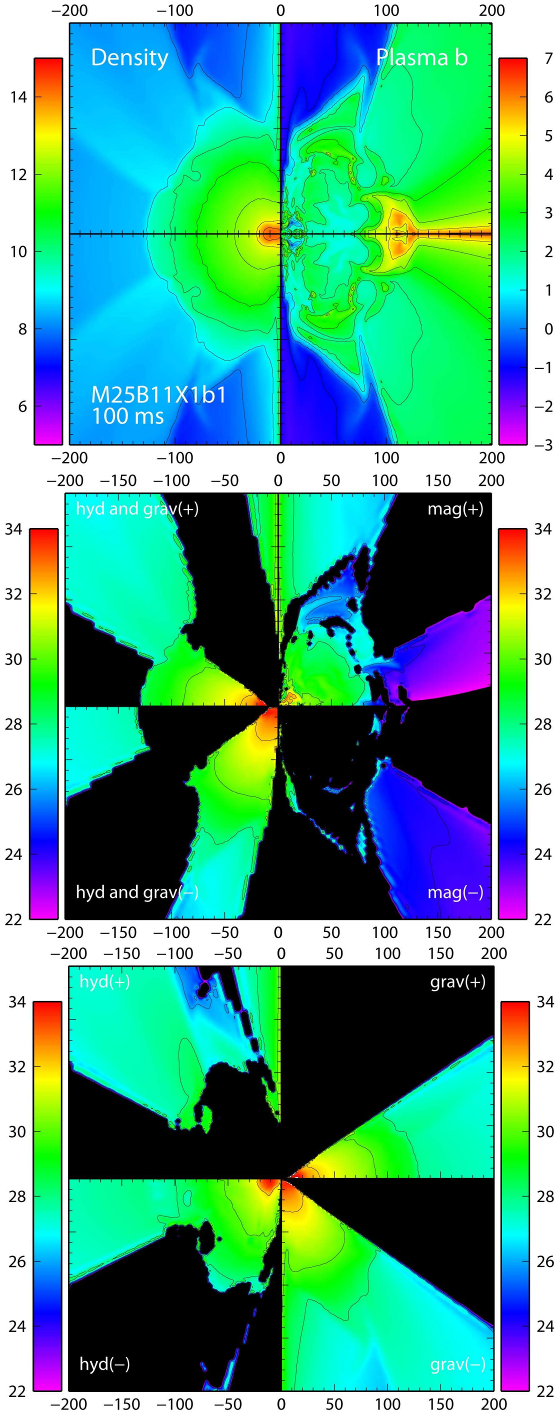

Fig. 5.— The top panel shows distributions of logarithm of density [g/cm^3] (left-half) and logarithm of β (right-half) for model B11X1β1 at 100 ms after bounce. Like Figure 2, the middle panel shows the sum of the hydrodynamic & gravitational part (left-half), while the magnetic contribution is shown in the right-half panel. The bottom panel is for the hydrodynamic (left-half) and gravity part (right-half), respectively. The side length of each plot is 400(km)x400(km). Compared to Figure 2, note that a more central region is focused here because the contribution to the GWs there are more important for the cancellation-type waveform.

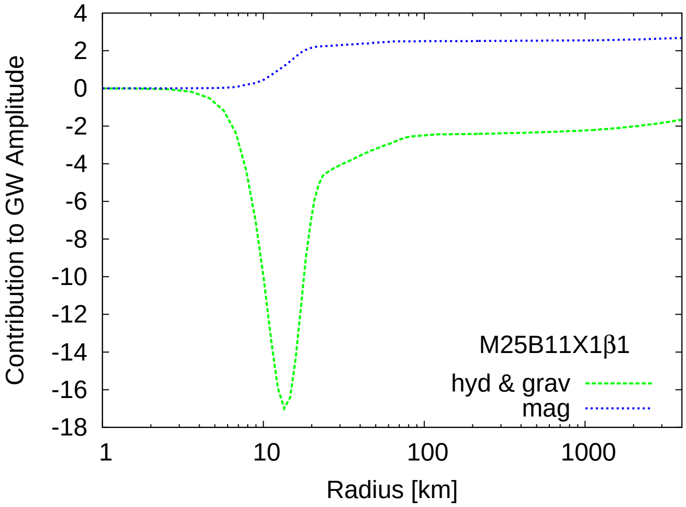

Fig. 6.— Same as Figure 3 but for model B11X1β1.

4.3. Spectrum Analysis

Now we move on to perform a spectral analysis (Figure 7). Both for the two types (left panel (increasing-type), right panel (cancellation-type)), the peak amplitudes in the spectra are around 1 kHz, which comes from the GWs near at bounce. It can be seen that the spectra for lower frequency domains (below $\sim$ 100 Hz) are much larger for the increasing type (left panels) compared to the cancellation type (right panels). This reflects a slower temporal variation of the secular drift inherent to the increase-type waveforms (e.g., Figure 1).

As a measure to characterize the dominance in the lower frequency domains, we define $\tilde{h}_{\rm low}$, which represents average amplitudes below 100 Hz (see Table 5). Although the peak amplitudes, $\tilde{h}_{\rm peak}$, in the spectra have no clear correlation with the two types, we point out that the final GW amplitudes (the first column) and the $\tilde{h}_{\rm low}$ (the third column) are much larger for the increasing type (colored by yellow) compared to the cancellation type (colored by light blue). In Figure 7, the peak amplitudes near 1 kHz are, irrespective of the two types, marginally within the detection limits of the currently running detector of the first LIGO and the detection seems more feasible for the next-generation detectors such as LCGT and the advanced LIGO for a Galactic supernova. It is true that the GWs in the low frequency domains mentioned above are relatively difficult to detect due to seismic noises, but a recently proposed future space interferometers like Fabry-Perot type DECIGO is designed to be sensitive in the frequency regimes (Kawamura et al. 2006; Kudoh et al. 2006). The sensitivity curve of the detector is plotted with the black line in Figure 7. Our results suggest that these low-frequency signals, if observed, could be one important messenger of the increase-type waveforms that are likely to be associated with MHD explosions exceeding 10^{51} erg.

5. Summary and Discussion

By performing a series of two-dimensional SRMHD simulations, we studied signatures of GWs in the MHD-driven core-collapse supernovae. In order to extract the gravitational waveforms, we presented a stress formula including contributions both from magnetic fields and special relativistic corrections. By changing the precollapse magnetic fields and initial angular momentum distributions parametrically, we computed twelve models. As for the microphysics, a realistic equation of state was employed and the neutrino cooling was taken into account via a multiflavor neutrino leakage scheme. With these computations, we found that the total GW amplitudes show a monotonic increase after bounce for models with a strong precollapse magnetic field (10^{12}G) also with a rapid rotation imposed. We pointed out

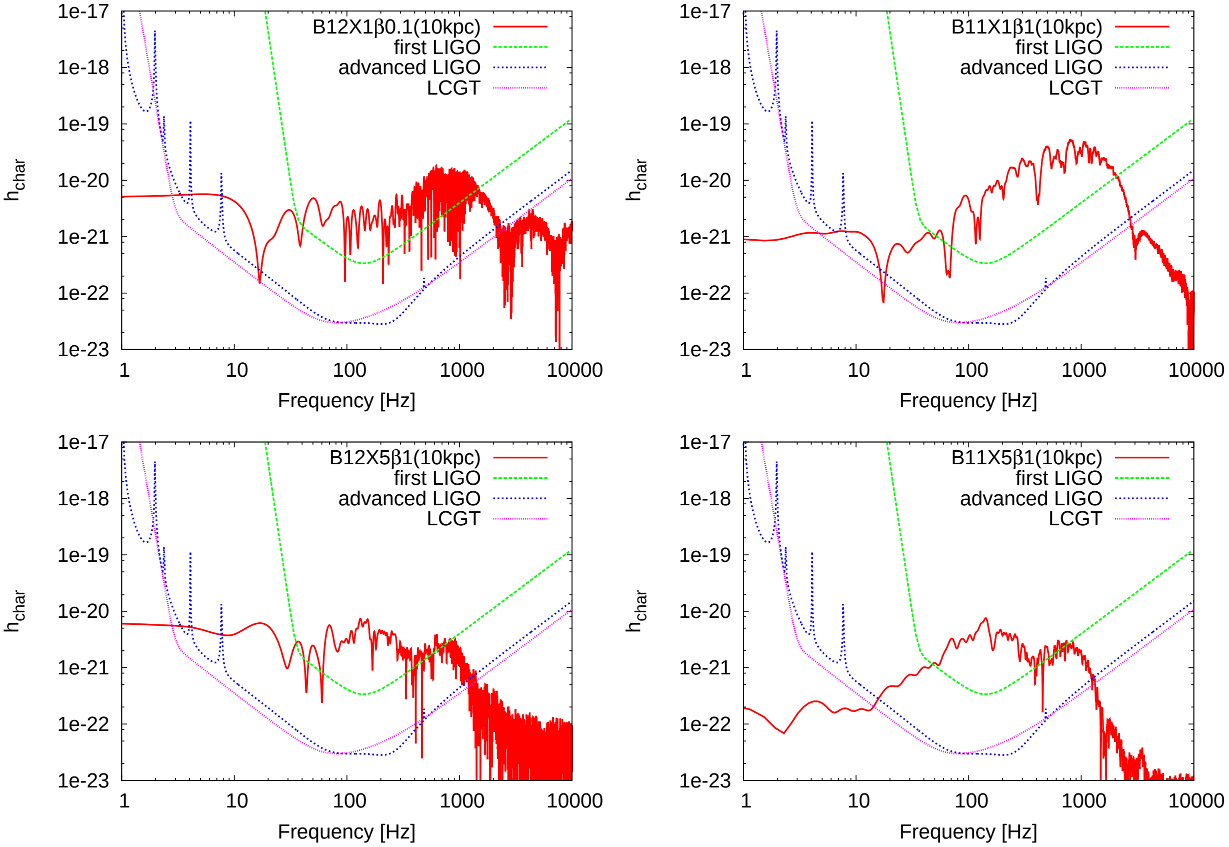

Fig. 7.— Gravitational-wave spectrum for representative models with the expected detection limits of the first LIGO (Abbott et al. 2005), the advanced LIGO (Weinstein 2002), Large-scale Cryogenic Gravitational wave Telescope (LCGT) (Kuroda & the LCGT Collaboration 2006), and Fabry-Perot type DECIGO (Kawamura et al. 2006; Kudoh et al. 2006). It is noted that $h_{\rm char}$ is the characteristic gravitational wave strain defined in Flanagan & Hughes (1998). The supernova is assumed to be located at the distance of 10 kpc.

Model	$h_{100\mathrm{ms}}[10^{-21}]$	$\tilde{h}_{\mathrm{peak}}[10^{-21}]$	$\tilde{h}_{\mathrm{low}}[10^{-21}]$
B11X1β0.1	2.2	10.3	0.3
B11X5β0.1	1.8	13.9	0.3
B11X20β0.1	2.0	3.0	0.3
B11X1β1	4.0	52.5	1.0
B11X5β1	0.8	7.5	0.2
B11X20β1	1.1	17.7	0.2
B12X1β0.1	22.0	18.1	5.2
B12X5β0.1	20.2	14.8	3.3
B12X20β0.1	3.5	8.2	0.9
B12X1β1	25.7	35.3	5.6
B12X5β1	26.3	7.4	4.8
B12X20β1	12.3	17.6	2.1

Table 5: Summary of GW amplitudes for all the models. The colors used for clarify are the same as Table 2. The first column represents the GW amplitudes when we terminated the simulation (100 ms after bounce). The second column, $\tilde{h}_{\mathrm{peak}}$, is the peak GW amplitudes in the spectra. The third column, $\tilde{h}_{\mathrm{low}}$, is the average amplitudes below 100 Hz. The supernova is assumed to be located at the distance of 10 kpc.

that this trend stems both from the kinetic contribution of MHD outflows with large radial velocities and also from the magnetic contribution dominated by the toroidal magnetic fields that predominantly trigger MHD explosions. For models with weaker initial magnetic fields, the total GW amplitudes after bounce stay almost zero, because the contribution from the magnetic fields cancels with the one from the hydrodynamic counterpart. These features can be clearly understood with a careful analysis on the explosion dynamics. It was pointed out that the GW signals with an increasing trend, possibly visible to the next-generation detectors for a Galactic supernova, would be associated with MHD explosions exceeding 10^{51} erg.

Although the presented simulations have utilized the leakage scheme to approximate the deleptonization, it would be more accurate (especially before bounce) to employ a formula developed by Liebendörfer (2005), which was designed to fit 1D Boltzmann results. Figure 8 shows snapshots at around 33 ms after bounce for model B12X20β0.1 in which the leakage scheme (left panel) or the Y_e prescription (right panel) is employed, respectively. Note that "G15" is taken in our simulation until bounce among the parameter sets in Liebendörfer (2005)[2] and is switched to the leakage scheme at the postbounce phase. As is shown, the

---

[2] The inner-core mass at bounce for the employed parameter set is 0.6 $M_\odot$ for our non-rotating 25 $M_\odot$ progenitor. This value is higher than that obtained in GR simulations (0.45-0.55 $M_\odot$) in Dimmelmeier et al. (2008). This may be because the pseudo GR potential employed in this work underestimates the GR gravity, which could potentially lead to a large inner-core mass.

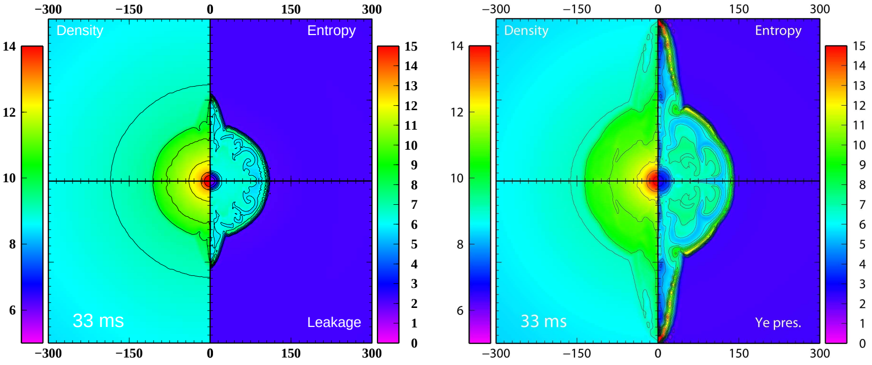

Fig. 8.— Snapshots at 33 ms after bounce for model B12X20β0.1 in which the leakage scheme (left panel) or the Y_e prescription (right panel) is employed, respectively. In each panel, density (logarithmic, left-half) and entropy (right-half) distributions are shown. The side length of each plot is 600x600(km).

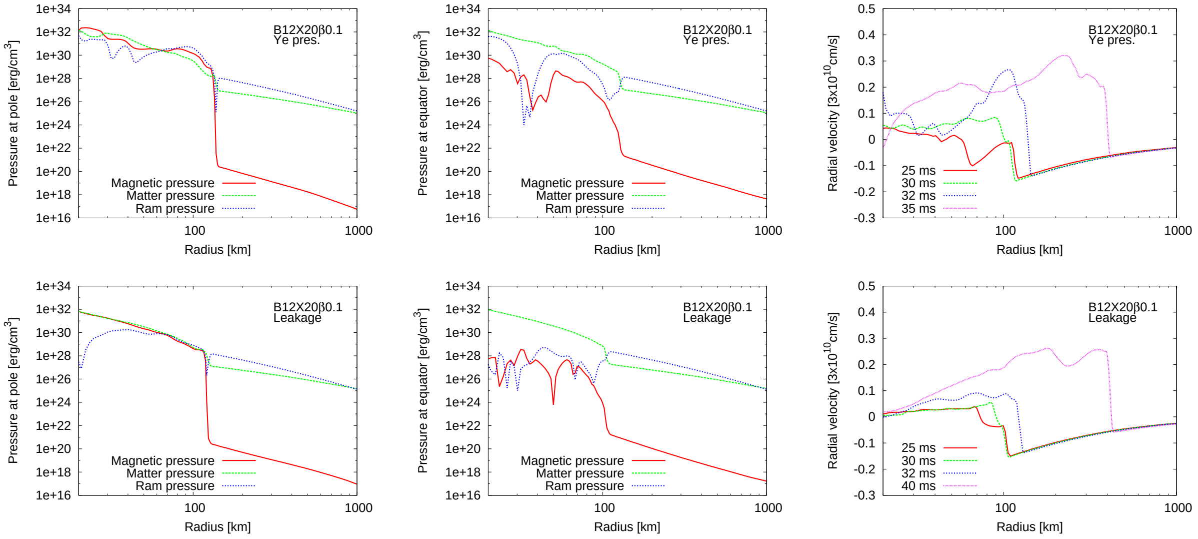

Fig. 9.— Left and middle panels show magnetic pressure (red line) vs. ram pressure (blue line) for model B12X20β0.1 around 32 ms after bounce with the Y_e prescription (top panels) or the leakage scheme (bottom panels) along the polar axis (left panel) or the equatorial plane (middle panel). Matter pressure is shown by green line as a reference. The right panels show velocity profiles along the pole near after the stall of the bounce shock (red lines). Both in the two different deleptonization schemes, the MHD-driven explosions are indeed obtained.

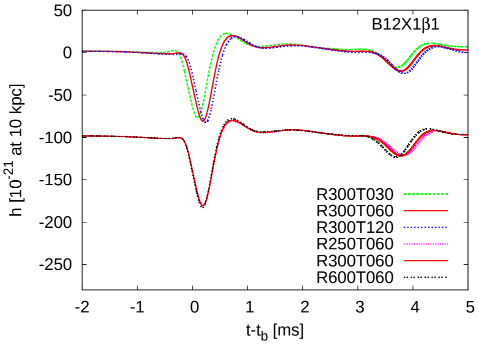

Fig. 10.— Gravitational waveforms for model B12X1β1 near bounce with different grid points. Three lines starting from 0 (at $t - t_{\rm b}$ = -2 ms with $t_{\rm b}$ being the epoch of bounce), correspond to models with different angular grid points (30 (green), 60(red), 120(blue)) while fixing the radial grid points to be 300. The bottom three lines are set to start from -100 in the GW amplitudes (just for convenience), and they correspond to models with different radial grid points (250 (pink), 300 (orange), 600 (brown)) while fixing the lateral grid points to be 60. Note that the fiducial set employed in this work is 300(r)x60(θ).

shock revival also occurs for the model with the Y_e prescription (right panel). Figure 9 depicts the magnetic pressure (red line) vs. ram pressure (blue line) along the polar axis (left panel) or the equatorial plane (middle) near the rebirth of the stalled shock for the model with the Y_e prescription (top panels) or the leakage scheme (bottom panels). For the equator, the magnetic pressure is much less than the ram pressure (middle panel), while the magnetic pressure amplified by the field wrapping along the pole becomes as high as the ram pressure of the infalling material at the shock front, leading to the MHD-driven shock formation (see right panels). Regardless of the two different deleptoniaztion schemes, these important features associated with the MHD explosions are shown to be quite similar.

Now we mention a comparison between the obtained results and relevant MHD simulations. Model R4E1CF in Scheidegger et al. (2010) whose precollapse rotational parameter is $\beta = 0.5$ % with a uniform rotation imposed, and whose initial poloidal magnetic field is set to 10^{12} G, is close to our model B12X20β0.1. From their Figure 23, the jet propagates to $\sim$ 300 km along the rotational axis at around $\sim$ 18 ms after bounce. In our counterpart model, the MHD-driven shock revives after around 30 ms after bounce, and it reaches to 300 km at around $\sim$ 10 ms, which is equivalent to $\sim$ 40 ms after bounce. Considering that our model ($\beta = 0.1\%$) is a slower rotator than model R4E1CF ($\beta = 0.5\%$), the delay of the shock revival for our model seems reasonable. Model s20A1B5-D3M12 in Cerdá-Durán et al. (2008) whose precollapse angular velocity is 4 rad/s (the rotational parameter should be close to

$\beta = 0.1$ %) with uniform rotation and whose initial poloidal magnetic field is 10^{12} G, is close to our model B12X20β0.1. From their Figure 10, the MHD jet propagates to ~ 240 km at 51 ms after bounce. The employed EOS is the same as ours (the Shen EOS), while the deleptonization scheme taken in their study was the Y_e formula (Liebendörfer 2005). As mentioned above, the dynamics is rather close to our corresponding model. Among the computed models in Burrows et al. (2007a), model M15B12DP2A1H which has a precollapse angular velocity of π rad/s (the rotational parameter should be close to $\beta = 0.06\%$) with initial dipolar magnetic field of 10^{12} G, is close to our model B12X20β0.1. The interval before the launch of the MHD shock for their model is 80 ms after bounce (e.g., their Table 1) is much later than our model (28 ms after bounce). This may be due to the larger initial angular momentum ($\beta = 0.1\%$) assumed in our study.

Model A3B3G5-D3M13 in Obergaulinger et al. (2005) which has a rotational parameter of $\beta = 0.9\%$ with a differential rotation imposed (the radial cut off is 500 km) and the initial poloidal magnetic field is 10^{13} G, is closer to our model B12X1β0.1. The MHD jet reaches to 500 km at around 7 ms after bounce, which is also the case of our counterpart model. As discussed above, our results are compatible to the ones obtained in the relevant foregoing results.

The major limitation of this study is the assumption of axisymmetry. Recently it was reported in three-dimensional (3D) MHD core-collapse simulations (Scheidegger et al. 2008, 2010) that the fast growth of the spiral SASI hinders the efficient amplification of the toroidal fields, which could suppress the formation of jets rather easily realized in 2D simulations. As a sequel of this study, we plan to investigate the 3D effects in SRMHD. Regarding a resolution dependence of our results, Figure 10 indicates that our standard resolution is adequate to follow the evolution of the computed models. However, it is not sufficient at all to capture the magneto-rotational instability (MRI, e.g., Balbus & Hawley (1998)). At least $10 - 100$ times finer mesh points are required for resolving the MRI (Obergaulinger et al. 2009), which may require some adaptive-mesh-refinement treatment, a very important component that remains to be improved. If the MRI could be resolved, the increasing-type waveform could emerge also for models with weakly initial magnetic fields because a more efficient field amplification could be captured. Although the general relativistic effects were treated only by a very approximative way, we think that the general relativity should not drastically change our results qualitatively, because the central protoneutron stars will not collapse to a black hole during our simulation time as inferred from a simple argument of the compactness of the inner-core. As for the microphysics, the neutrino heating is not included in this study. However the inclusion of the neutrino heating may play a minor role in the waveforms, since the timescales before the neutrino-driven explosions set in (e.g., Marek & Janka (2009); Bruenn et al. (2010); Suwa et al. (2009) and references therein) are much longer than the

MHD explosions.

As one possible extension of this study, we think it interesting to study GWs from anisotropic neutrino radiation in the MHD models. Extrapolating the outcome obtained in previous studies (e.g., Müller et al. (2004); Kotake et al. (2009a)), we anticipate that the total amplitudes become larger when we include the neutrino GWs. This is because the neutrino GWs may make a positive contribution since the neutrino emissions from the oblately deformed protoneutron stars become stronger toward the polar direction (Janka & Moenchmeyer 1989; Kotake et al. 2003a; Walder et al. 2005; Ott et al. 2008). If this is really the case, the total GW amplitudes especially for the increasing type should be much larger, possibly making its detection more promising. Furthermore, the neutrino signals from MHD explosions, may have a sharp directional dependence through neutrino oscillations, reflecting the aspherical propagation of the shock to the stellar envelope (Kawagoe et al. 2009). Taking a correlation analysis between the neutrino and GW signals could help to reveal the hidden nature of the central engines. In fact, several observational proposals have been made in this direction recently (van Elewyck et al. 2009; Aso et al. 2008; Leonor et al. 2010). The MHD-driven core-collapse supernovae, albeit rather minor among typical type II supernova explosions, seem to still contain a number of rich research subjects.

We are grateful to K. Sato and S. Yamada for continuing encouragements. We also thank to our anonymous referee for a number of suggestions which helped us a lot to improve our manuscript. Numerical computations were in part carried on XT4 and general common use computer system at the center for Computational Astrophysics, CfCA, the National Astronomical Observatory of Japan. This study was supported in part by the Grants-in-Aid for the Scientific Research from the Ministry of Education, Science and Culture of Japan (Nos. 19104006, 19540309 and 20740150).

REFERENCES

Abbott et al., M. 2005, Phys. Rev. D, 72, 122004

Ando, M. & the TAMA Collaboration. 2005, Classical and Quantum Gravity, 22, 881

Ardeljan, N. V., Bisnovatyi-Kogan, G. S., & Moiseenko, S. G. 2000, Astron. Astrophys., 355, 1181

Aso, Y., Márka, Z., Finley, C., Dwyer, J., Kotake, K., & Márka, S. 2008, Classical and Quantum Gravity, 25, 114039

Balbus, S. A. & Hawley, J. F. 1998, Reviews of Modern Physics, 70, 1

Bionta, R. M., Blewitt, G., Bratton, C. B., Caspere, D., & Ciocio, A. 1987, Physical Review Letters, 58, 1494

Blanchet, L., Damour, T., & Schaefer, G. 1990, MNRAS, 242, 289

Bruenn, S. W., Mezzacappa, A., Hix, W. R., Blondin, J. M., Marronetti, P., Messer, O. E. B., Dirk, C. J., & Yoshida, S. 2010, ArXiv e-prints

Buras, R., Rampp, M., Janka, H.-T., & Kifonidis, K. 2006, A&A, 447, 1049

Burrows, A., Dessart, L., Livne, E., Ott, C. D., & Murphy, J. 2007a, Astrophys. J., 664, 416

Burrows, A. & Hayes, J. 1996, Physical Review Letters, 76, 352

Burrows, A., Livne, E., Dessart, L., Ott, C. D., & Murphy, J. 2006, Astrophys. J., 640, 878

—. 2007b, Astrophys. J., 655, 416

Cerdá-Durán, P., Font, J. A., Antón, L., & Müller, E. 2008, Astron. Astrophys., 492, 937

Cerdá-Durán, P., Font, J. A., & Dimmelmeier, H. 2007, A&A, 474, 169

De Villiers, J.-P., Hawley, J. F., & Krolik, J. H. 2003, Astrophys. J., 599, 1238

Dimmelmeier, H., Font, J. A., & Müller, E. 2002a, Astron. Astrophys., 393, 523

Dimmelmeier, H., Font, J. A., & Müller, E. 2002b, A&A, 393, 523

Dimmelmeier, H., Ott, C. D., Janka, H.-T., Marek, A., & Müller, E. 2007, Physical Review Letters, 98, 251101

Dimmelmeier, H., Ott, C. D., Marek, A., & Janka, H. 2008, Phys. Rev. D, 78, 064056

Epstein, R. I. & Pethick, C. J. 1981, Astrophys. J., 243, 1003

Finn, L. S. & Evans, C. R. 1990, Astrophys. J., 351, 588

Flanagan, É. É. & Hughes, S. A. 1998, Phys. Rev. D, 57, 4566

Fryer, C. L. 2004, Astrophys. J. Lett., 601, L175

Fuller, G. M., Fowler, W. A., & Newman, M. J. 1985, Astrophys. J., 293, 1

Harikae, S., Kotake, K., & Takiwaki, T. 2010, Astrophys. J., 713, 304

Harikae, S., Takiwaki, T., & Kotake, K. 2009, Astrophys. J., 704, 354

Heger, A. & Langer, N. 2000, Astrophys. J., 544, 1016

Hirata, K., Kajita, T., Koshiba, M., Nakahata, M., & Oyama, Y. 1987, Physical Review Letters, 58, 1490

Hough, J., Rowan, S., & Sathyaprakash, B. S. 2005, Journal of Physics B Atomic Molecular Physics, 38, 497

Itoh, N., Adachi, T., Nakagawa, M., Kohyama, Y., & Munakata, H. 1989, Astrophys. J., 339, 354

—. 1990, Astrophys. J., 360, 741

Janka, H. & Moenchmeyer, R. 1989, A&A, 209, L5

Kawagoe, S., Takiwaki, T., & Kotake, K. 2009, Journal of Cosmology and Astro-Particle Physics, 9, 33

Kawamura, S., Nakamura, T., Ando, M., Seto, N., Tsubono, K., Numata, K., Takahashi, R., Nagano, S., Ishikawa, T., Musha, M., Ueda, K., Sato, T., Hosokawa, M., Agatsuma, K., Akutsu, T., Aoyanagi, K., Arai, K., Araya, A., Asada, H., Aso, Y., Chiba, T., Ebisuzaki, T., Eriguchi, Y., Fujimoto, M., Fukushima, M., Futamase, T., Ganzu, K., Harada, T., Hashimoto, T., Hayama, K., Hikida, W., Himemoto, Y., Hirabayashi, H., Hiramatsu, T., Ichiki, K., Ikegami, T., Inoue, K. T., Ioka, K., Ishidoshiro, K., Itoh, Y., Kamagasako, S., Kanda, N., Kawashima, N., Kirihara, H., Kiuchi, K., Kobayashi, S., Kohri, K., Kojima, Y., Kokeyama, K., Kozai, Y., Kudoh, H., Kunimori, H., Kuroda, K., Maeda, K., Matsuhara, H., Mino, Y., Miyakawa, O., Miyoki, S., Mizusawa, H., Morisawa, T., Mukohyama, S., Naito, I., Nakagawa, N., Nakamura, K., Nakano, H., Nakao, K., Nishizawa, A., Niwa, Y., Nozawa, C., Ohashi, M., Ohishi, N., Ohkawa, M., Okutomi, A., Oohara, K., Sago, N., Saijo, M., Sakagami, M., Sakata, S., Sasaki, M., Sato, S., Shibata, M., Shinkai, H., Somiya, K., Sotani, H., Sugiyama, N., Tagoshi, H., Takahashi, T., Takahashi, H., Takahashi, R., Takano, T., Tanaka, T., Taniguchi, K., Taruya, A., Tashiro, H., Tokunari, M., Tsujikawa, S., Tsunesada, Y., Yamamoto, K., Yamazaki, T., Yokoyama, J., Yoo, C., Yoshida, S., & Yoshino, T. 2006, Classical and Quantum Gravity, 23, 125

Kotake, K., Iwakami, W., Ohnishi, N., & Yamada, S. 2009a, Astrophys. J., 704, 951

—. 2009b, Astrophys. J. Lett., 697, L133

Kotake, K., Iwakami-Nakano, W., & Ohnishi, N. 2011, ApJ, 736, 124

Kotake, K., Ohnishi, N., & Yamada, S. 2007, Astrophys. J., 655, 406

Kotake, K., Sato, K., & Takahashi, K. 2006, Reports of Progress in Physics, 69, 971

Kotake, K., Sawai, H., Yamada, S., & Sato, K. 2004a, Astrophys. J., 608, 391

Kotake, K., Yamada, S., & Sato, K. 2003a, Astrophys. J., 595, 304

—. 2003b, Phys. Rev. D, 68, 044023

—. 2005, ApJ, 618, 474

Kotake, K., Yamada, S., Sato, K., Sumiyoshi, K., Ono, H., & Suzuki, H. 2004b, Phys. Rev. D, 69, 124004

Kudoh, H., Taruya, A., Hiramatsu, T., & Himemoto, Y. 2006, Phys. Rev. D, 73, 064006

Kuroda, K. & the LCGT Collaboration. 2006, Classical and Quantum Gravity, 23, 215

Leonor, I., Cadonati, L., Coccia, E., D'Antonio, S., Di Credico, A., Fafone, V., Frey, R., Fulgione, W., Katsavounidis, E., Ott, C. D., Pagliaroli, G., Scholberg, K., Thrane, E., & Vissani, F. 2010, Classical and Quantum Gravity, 27, 084019

Liebendörfer, M. 2005, ApJ, 633, 1042

Marek, A. & Janka, H.-T. 2009, Astrophys. J., 694, 664

Marek, A., Janka, H.-T., & Müller, E. 2009, Astron. Astrophys., 496, 475

Meszaros, P. 2006, Reports of Progress in Physics, 69, 2259

Mönchmeyer, R., Schaefer, G., Mueller, E., & Kates, R. E. 1991, Astron. Astrophys., 246, 417

Müler, E. & Janka, H.-T. 1997, Astron. Astrophys., 317, 140

Müller, E., Rampp, M., Buras, R., Janka, H.-T., & Shoemaker, D. H. 2004, Astrophys. J., 603, 221

Murphy, J. W., Ott, C. D., & Burrows, A. 2009, ApJ, 707, 1173

Obergaulinger, M., Aloy, M. A., Dimmelmeier, H., & Müller, E. 2006a, Astron. Astrophys., 457, 209

Obergaulinger, M., Aloy, M. A., & Müller, E. 2006b, Astron. Astrophys., 450, 1107

Obergaulinger, M., Cerdá-Durán, P., Müller, E., & Aloy, M. A. 2009, A&A, 498, 241

Ott, C. D. 2009, Classical and Quantum Gravity, 26, 063001

Ott, C. D., Burrows, A., Dessart, L., & Livne, E. 2006, Physical Review Letters, 96, 201102

—. 2008, ApJ, 685, 1069

Ott, C. D., Burrows, A., Livne, E., & Walder, R. 2004, Astrophys. J., 600, 834

Ott, C. D., Dimmelmeier, H., Marek, A., Janka, H., Hawke, I., Zink, B., & Schnetter, E. 2007a, Physical Review Letters, 98, 261101

Ott, C. D., Dimmelmeier, H., Marek, A., Janka, H., Zink, B., Hawke, I., & Schnetter, E. 2007b, Classical and Quantum Gravity, 24, 139

Rosswog, S. & Liebendörfer, M. 2003, MNRAS, 342, 673

Scheck, L., Janka, H., Foglizzo, T., & Kifonidis, K. 2008, A&A, 477, 931

Scheck, L., Plewa, T., Janka, H.-T., Kifonidis, K., & Müller, E. 2004, Physical Review Letters, 92, 011103

Scheidegger, S., Fischer, T., Whitehouse, S. C., & Liebendörfer, M. 2008, Astron. Astrophys., 490, 231

Scheidegger, S., Käppeli, R., Whitehouse, S. C., Fischer, T., & Liebendörfer, M. 2010, A&A, 514, A51+

Shen, H., Toki, H., Oyamatsu, K., & Sumiyoshi, K. 1998, Nuclear Physics A, 637, 435

Shibata, M., Liu, Y. T., Shapiro, S. L., & Stephens, B. C. 2006, Phys. Rev. D, 74, 104026

Shibata, M. & Sekiguchi, Y.-I. 2004, Phys. Rev. D, 69, 084024

Suwa, Y., Kotake, K., Takiwaki, T., Whitehouse, S. C., Liebendoerfer, M., & Sato, K. 2009, ArXiv e-prints

Takahashi, K., El Eid, M. F., & Hillebrandt, W. 1978, Astron. Astrophys., 67, 185

Takiwaki, T., Kotake, K., Nagataki, S., & Sato, K. 2004, Astrophys. J., 616, 1086

Takiwaki, T., Kotake, K., & Sato, K. 2009, Astrophys. J., 691, 1360

Thorne, K. S. 1980, Reviews of Modern Physics, 52, 299

van Elewyck, V., Ando, S., Aso, Y., Baret, B., Barsuglia, M., Bartos, I., Chassande-Mottin, E., di Palma, I., Dwyer, J., Finley, C., Kei, K., Kouchner, A., Marka, S., Marka, Z., Rollins, J., Ott, C. D., Pradier, T., & Searle, A. 2009, International Journal of Modern Physics D, 18, 1655

Walder, R., Burrows, A., Ott, C. D., Livne, E., Lichtenstadt, I., & Jarrah, M. 2005, ApJ, 626, 317

Weinstein, A. 2002, Classical and Quantum Gravity, 19, 1575

Woosley, S. E. & Bloom, J. S. 2006, ARA&A, 44, 507

Woosley, S. E. & Heger, A. 2006, Astrophys. J., 637, 914

Yamada, S. & Sawai, H. 2004, Astrophys. J., 608, 907

Yoon, S.-C. & Langer, N. 2005, Astron. Astrophys., 443, 643

Zwerger, T. & Mueller, E. 1997, Astron. Astrophys., 320, 209

This preprint was prepared with the AAS LaTeX macros v5.2.